Inorganic Chemistry

Article

pubs.acs.org/IC

Trimethylsulfonium Lead Triiodide: An Air-Stable Hybrid Halide Perovskite

Andreas Kaltzoglou,[†] Constantinos C. Stoumpos,[‡] Athanassios G. Kontos,[†] Georgios K. Manolis,[†] Kyriakos Papadopoulos,[†] Kyriaki G. Papadokostaki,[†] Vasilis Psycharis,[†] Chiu C. Tang,[§] Young-Kwang Jung,[∥] Aron Walsh,[∥,⊥] Mercouri G. Kanatzidis,[‡] and Polycarpos Falaras*[,†]

[†]Institute of Nanoscience and Nanotechnology, National Center for Scientific Research "Demokritos", 15310, Agia Paraskevi Attikis, Athens, Greece

[‡]Department of Chemistry, Northwestern University, Evanston, Illinois 60208, United States

[§]Diamond Light Source, Harwell Science and Innovation Campus, Didcot, Oxfordshire OX11 0DE, United Kingdom

[∥]Global E3 Institute and Department of Materials Science and Engineering, Yonsei University, Seoul 120-749, Korea

[⊥]Department of Materials, Imperial College London, Exhibition Road, London SW7 2AZ, United Kingdom

Supporting Information

ABSTRACT: We report on the synthesis, characterization, and optoelectronic properties of the novel trimethylsulfonium lead triiodide perovskite, $(CH_3)_3SPbI_3$. At room temperature, the air-stable compound adopts a hexagonal crystal structure with a 1D network of face-sharing $[PbI_6]$ octahedra along the *c* axis. UV−vis reflectance spectroscopy on a pressed pellet revealed a band gap of 3.1 eV, in agreement with first-principles calculations, which show a small separation between direct and indirect band gaps. Electrical resistivity measurements on single crystals indicated that the compound behaves as a semiconductor. According to multi-temperature single-crystal X-ray diffraction, synchrotron powder X-ray diffraction, Raman spectroscopy, and differential scanning calorimetry, two fully reversible structural phase transitions occur at −5 and ca. −100 °C with reduction of the unit cell symmetry to monoclinic as temperature decreases. The role of the trimethylsulfonium cation regarding the chemical stability and optoelectronic properties of the new compound is discussed in comparison with $APbI_3$ (A = Cs, methylammonium, and formamidinium cation), which are most commonly used in perovskite solar cells.

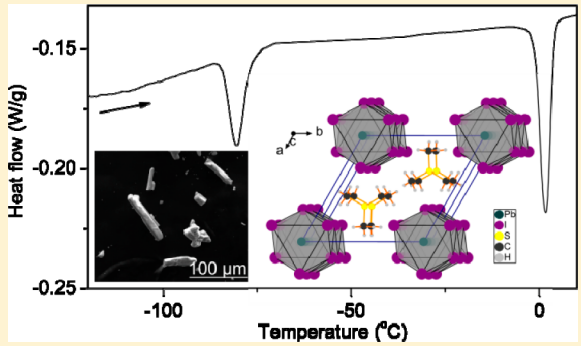

1. INTRODUCTION

Perovskites constitute a large class of compounds with diverse chemical composition and structural modifications of the cubic ABX_3 archetype (e.g., $SrTiO_3$).[1] Different application fields for materials with perovskite-related structures have been developed such as ferroelectrics (e.g., $BaTiO_3$[2]), ferromagnets (e.g., $(La,Sr)MnO_3$[3]), superconductors (e.g., $YBa_2Cu_3O_7$[4]), thermoelectrics (e.g., $Yb_{0.2}CoSb_3$ skutterudite[5]), luminescent materials and light-emitting diodes (e.g., $(4\text{-fluorophenethylamine-H})_2PbI_4$[6] and $CsPbBr_3$ nanocrystals[7]), and more recently as hole-transporting materials (HTMs) (e.g., $CsSnI_3$[8]) in dye-sensitized solar cells (DSSCs) and as light absorbers in perovskite solar cells (e.g., $CH_3NH_3PbI_3$[9,10]). In particular, the use of hybrid organic−inorganic lead halides as active layers in this new type of third generation photovoltaic devices has received great attention, and power conversion efficiency (PCE) values of over 20% have been achieved.[11]

There is a wealth in choice of organic cations (A) that can be used in the $APbI_3$ structure with different shape, size, polarizability, and electronegativity.[12,13] The tolerance factor (t) is a useful tool to predict the structure type of the perovskite. Values in the range of $0.8 < t < 1$ favor 3D structures with edge-sharing $[PbI_6]$ octahedra (e.g., $CH_3NH_3PbI_3$). For $t < 0.8$, the NH_4CdCl_3-type structure is formed, whereas for $t > 1$, 1D or 2D structures with face-sharing $[PbI_6]$ octahedra are formed.[14−19] Such low-dimensionality perovskites are also good candidates for tandem solar cells,[20] and it was recently observed that the 2D semiconducting $(CH_3(CH_2)_3NH_3)_2(CH_3NH_3)_{n-1}Pb_nI_{3n+1}$ (n = 1, 2, 3, 4) compounds exhibit good long-term stability in air while maintaining their efficiency in perovskite solar cells.[21]

Our aim is to expand the, so far, limited variety of organic cations by exploring sulfur-based analogues as stable moieties against humidity that could ultimately be incorporated in solar cells and improve their performance either as light absorbers or as HTMs. We investigate here the role of the trimethylsulfonium cation in the $APbI_3$ structure as an alternative to the well-studied inorganic (e.g., Cs^+) and organic (e.g., methylammonium (MA) and formamidinium (FA)) cations.[22,23]

Received: February 15, 2017
Published: May 16, 2017

DOI: 10.1021/acs.inorgchem.7b00395
Inorg. Chem. 2017, 56, 6302−6309

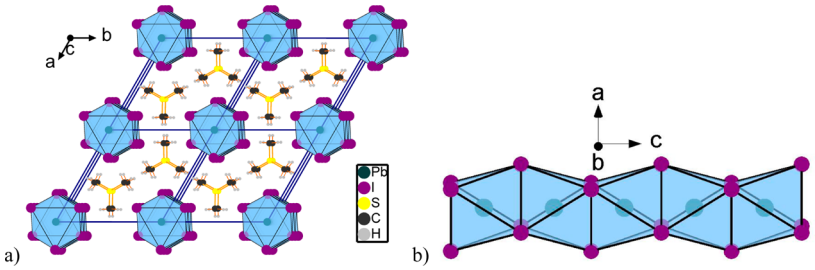

Figure 1. Crystal structure of $(CH_3)_3SPbI_3$ at room temperature: (a) (001) view of 2 × 2 × 2 unit cell and (b) (010) view of the face-sharing $[PbI_6]$ octahedra.

2. EXPERIMENTAL SECTION

The new perovskite was prepared in two steps. First, equimolar amounts of CH_3I and $(CH_3)_2S$ reacted at room temperature for 12 h. White crystals of $(CH_3)_3SI$ were formed and washed twice with diethyl ether.[24] Second, equimolar amounts of $(CH_3)_3SI$ and PbI_2 (Aldrich, 99.999%) reacted in *N*,*N*-dimethylformamide (DMF) solution at 60 °C for 2 h. The slightly soluble $(CH_3)_3SPbI_3$ product was isolated by filtration in the form of yellow needle-like crystals (Figure S1) and was washed twice with diethyl ether. The sample that was prepared in DMF solution was used for all experimental analyses mentioned below, except for single-crystal X-ray diffraction. For the latter experiment, suitable crystals were grown by layering 2 mL of an aqueous solution of $(CH_3)_3SI$ (67 mg, 0.33 mmol) on top of a solution of PbO (74 mg, 0.33 mmol) in 10 mL of concentrated HI (57% w/w). Crystals of the title compound grew overnight upon mixing of the solvents, forming thin platelets with a hexagonal crystal habit.

Scanning electron microscopy (SEM) of the perovskite polycrystalline powder was performed on a Quanta 200 SEM instrument by accelerating the electron beam at 25 kV (Figure S1).

The air-stable compound was thoroughly ground in an agate mortar and was structurally characterized by X-ray powder diffraction (XRPD) using a Siemens D-500 diffractometer that operates in Bragg–Brentano geometry with Cu Kα1 (λ = 1.5406 Å) and Cu Kα2 (λ = 1.5444 Å) radiation. Data were collected over the angular range $5° \leq 2\theta \leq 100°$ counting for 3 s at each step of 0.02° in detector position. Single-crystal X-ray diffraction experiments were performed using a STOE IPDS II image-plate diffractometer equipped with a Mo Kα radiation (λ = 0.71073 Å) source, operating at 50 kV and 40 mA. Selected crystals were collected at 20 and −50 °C using an Oxford Cryostream Plus cryostat. Integration and numerical absorption correction were performed using the X-RED and X-SHAPE programs, respectively, found in the X-Area program suite. The structures were solved by charge-flipping and refined by full-matrix least-squares on F^2 using the Jana2006 program package.[25] The TwinRotMat functions of PLATON software[26] were used to identify the twinning domains and validate chosen space group for the low-temperature crystal structure.

High-resolution synchrotron X-ray powder diffraction (SXPD) was also performed on a sample at room and low temperatures using Beamline I11 at Diamond Light Source, UK.[27] The polycrystalline sample was loaded into a 0.5 mm diameter capillary (borosilicate glass), and SXPD patterns were recorded each with a 10 s exposure using a position-sensitive Mythen-II detector (90° aperture and 0.004° 2θ interval).[28] The wavelength of λ = 0.82612(2) Å was calibrated using a pattern from a high-quality silicon powder standard (SRM640c), and a cryostream (−193 to 227 °C) was used for the control of sample temperatures. Four data sets were collected at 22, −50, −120, and again at 22 °C. Rietveld refinements were carried out using the FULLPROF software.[29]

Differential scanning calorimetry (DSC) was carried out on a DSC2920 device (TA Instruments). The sample was placed in a sealed Al pan, and data were recorded under continuous N_2 flow. Separate measurements were performed over the temperature ranges of −150 to 20 °C and −20 to 330 °C. A heating/cooling rate of 3 °C min^{-1} was kept for all runs. The residues of the thermal analysis were further monitored with the above-mentioned XRPD method.

UV–vis spectra were recorded on a Hitachi U-3010 spectrophotometer equipped with an integrating sphere. Polycrystalline powder of $(CH_3)_3SPbI_3$ was pressed into a 10 mm diameter × ca. 1 mm thick pellet in stainless steel dies. The pellet was measured in diffuse reflectance (R) mode, and the band gap was determined using the Kubelka–Munk equation: $F(R) = (1 - R)^2/2R$.[30]

Electrical resistivity was recorded using a Keithley 6517B electrometer using a standard two-probe contact geometry. A graphite suspension in 2-propanol was used as an electrical contact between the Cu wires and the single-crystal samples. A needle-shaped crystal grown from the DMF solution with dimensions of 1.3 mm (length) and 0.2 × 0.2 mm^2 (cross section) and a hexagonal plate-like crystal grown from the aqueous solution with dimensions of 0.1 mm (length) and 0.1 × 0.03 mm^2 (cross section) were used for the charge-transport characterization of the compound.

Micro-Raman spectra were measured for both $(CH_3)_3SPbI_3$ and the $(CH_3)_3SI$ precursor in the 30–3200 cm^{-1} range in backscattering configuration on a dispersive Renishaw in-Via Reflex spectrometer with 250 mm focal length equipped with a high sensitivity, deep-depletion CCD detector. The samples were loaded into a THMS600PS Linkam temperature-controlled heating–freezing optical stage under an inert argon atmosphere for measurements over the temperature range of −193 to 220 °C. Excitation was performed by a near-infrared (NIR) solid-state laser emitting at a wavelength of 785 nm. The laser beam was focused on the sample's surface using a 50× long-focal-distance objective lens of a Leica DMLM microscope providing power density of approximately 1 mW/μm^2. Raman scattered signal was filtered by a 30 cm^{-1} cutoff dielectric filter and analyzed with a 1200 lines/mm diffraction grating. Measurements were carried out with circular polarization of the incident laser beam on $(CH_3)_3SPbI_3$ crystals aligned at 45° relative to the direction of the spectrometer slit in order to record unpolarized Raman spectra. Spectral deconvolution was carried out by linear least-squares fitting of the Raman peaks to a mixture of Lorentzian and Gaussian line shapes.

First-principles electronic structure calculations were performed within Kohn–Sham density functional theory (DFT), as implemented in the Vienna Ab initio Simulation Package (VASP). Projector-augmented wave (PAW) pseudopotentials are used to treat semicore electronic states with the Pb 5d band included explicitly as valence.[31,32] Electron exchange and correlation were described within the generalized gradient approximation (GGA) of Perdew, Burke, and Ernzerhof revised for solids (PBEsol).[33] For more quantitative estimate of the band gap, spin–orbit was included for the electronic band structure calculation, which reduced the calculated band gap from 3.03 to 2.59 eV. The plane-wave kinetic energy cutoff was set to 700 eV with a k-point sampling mesh of 6 × 6 × 8 (structure optimization) and 8 × 8 × 10 (dielectric functions).

3. RESULTS AND DISCUSSION

3.1. Structural Analysis. Single-crystal X-ray diffraction analysis showed that the reaction product crystallizes at room temperature with hexagonal symmetry in the space group $P6_3mc$ (no. 186). The distorted, face-sharing $[PbI_6]$ polyhedra

DOI: 10.1021/acs.inorgchem.7b00395
Inorg. Chem. 2017, 56, 6302–6309

form 1D chains along the *c* axis (Figure 1 and Tables S1−S4). This resembles the *δ*-modification of $FAPbI_3$, which is also yellow and thermodynamically stable at room temperature.[34,35] The trimethylsulfonium cations occupy interstitial sites between the distorted, face-sharing $[PbI_6]$ octahedra. Due to the larger volume of $(CH_3)_3S^+$ compared to the formamidinium cation, $a = b$ lattice parameters are 10.5% larger in $(CH_3)_3SPbI_3$ than in *δ*-$FAPbI_3$, whereas *c* parameter is only larger by 1% (Table 1). As a result, the crystallographic density of

Table 1. Crystallographic Data and Refinement Parameters for $(CH_3)_3SPbI_3$ from Single-Crystal X-ray Diffraction Data at 20 and −50 °C[a]

compound	$C_3H_9SPbI_3$	
formula weight (g mol^{-1})	665.1	
diffractometer	STOE IPDS II	
wavelength (Å)	0.71073	
temperature (°C)	20	−50
space group	$P6_3mc$ (no. 186)	Cc (no. 9)
Z	2	8
unit cell parameters, a (Å)	9.5635(9)	15.3491(19)
unit cell parameters, b (Å)	9.5635(9)	10.0434(8)
unit cell parameter, c (Å)	7.9795(8)	15.9420(19)
unit cell parameter, α (deg)	90	90
unit cell parameter, β (deg)	90	95.425(10)
unit cell parameter, γ (deg)	120	90
unit cell volume, V (Å^3)	632.03(10)	2446.6(5)
$\rho_{calcd.}$ (g cm^{-3})	3.49462	3.6112
absorption coeff., μ (mm^{-1})	20.778	21.471
$F(000)$	568	2272
θ range (deg)	2.46 to 25.19	2.43 to 25.28
no. of integrated reflections	3882	7567
no. of independent reflections	443 [R_{int} = 0.0458]	2849 [R_{int} = 0.09]
no. of data/restraints/parameters	443/3/21	2849/12/113
goodness-of-fit on F^2	2.51	1.99
refinement method	full-matrix least-squares on F^2	
final R indices [$I > 2\sigma(I)$]	R_{obs} = 0.0433	R_{obs} = 0.0683
	wR_{obs} = 0.0978	wR_{obs} = 0.1327
final R indices [all data]	R_{all} = 0.0564	R_{all} = 0.0968
	wR_{all} = 0.0993	wR_{all} = 0.1359
extinction coefficient	0.027(1)	
residual map/e Å^{-3}	1.01 and −0.87	3.23 and −1.99

[a] $R = \sum||F_o| - |F_c||/\sum|F_o|$, $wR = \{\sum[w(|F_o|^2 - |F_c|^2)^2]/\sum[w(|F_o|^4)]\}^{1/2}$ and $w = 1/(\sigma^2(I) + 0.0004I^2)$.

$(CH_3)_3SPbI_3$ (3.49 g cm^{-3}) is significantly lower than that in all other known modifications of $MAPbI_3$ and $FAPbI_3$ (including *δ*-$FAPbI_3$), with values of 4.1−4.3 g cm^{-3},[34] but rather close to the density of $((CH_3)_3NH)PbI_3$ (3.55 g cm^{-3}).[36]

Similarly to other halide perovskites and "perovskitoids", $(CH_3)_3SPbI_3$ undergoes a series of structural phase transitions following the relaxation of the crystal structure from a dynamically disordered state to a static crystal structure (Figure 2 and Tables 1 and S5−S8). The first transition occurs at −5 °C and results in the lowering of the symmetry to the polar monoclinic space group *Cc* (no. 9). The monoclinic unit cell axes take approximate values that resemble that of the orthohexagonal C cell[37] with double c_{hex} axis ($\mathbf{a}_{mono} = -2\mathbf{a}_{mono} - \mathbf{b}_{mono}$, $\mathbf{b}_{mono} = \mathbf{b}_{hex}$, $\mathbf{c}_{mono} = -2\mathbf{c}_{hex}$). The *β*-phase of $(CH_3)_3SPbI_3$, which exists between −5 and −120 °C, has the same face-sharing topology with the room temperature phase,

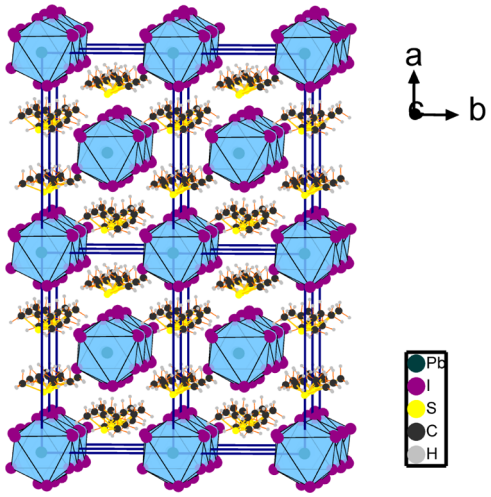

Figure 2. Crystal structure of $(CH_3)_3SPbI_3$ at −50 °C in (001) view of the 2 × 2 × 2 unit cell.

with the important difference that the adjacent octahedra have rotated by ∼10° with respect to the former 6_3 screw axis. The change in the alignment of the iodoplumbate octahedra is accompanied by a concomitant change in the orientation of the trimethylsulfonium cations which, in this instance, are aligned vertically to the crystallographic *c* axis. A *γ*-phase also appears to exist below −120 °C, although it was not possible to determine the crystal structure due to extensive twinning that precludes the determination of the correct unit cell.

The above-mentioned phase transitions were also observed in the multi-temperature SXPD patterns (Figure 3). The *β*-

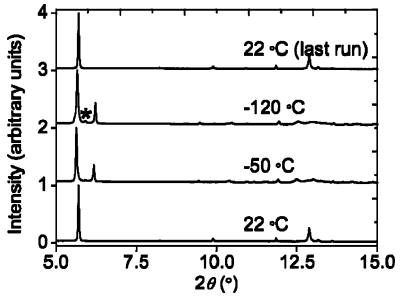

Figure 3. Intensity-normalized synchrotron powder diffraction patterns for $(CH_3)_3SPbI_3$ at room temperature and nonambient temperatures. Three distinct phases are observed. The transitions are fully reversible.

phase of $(CH_3)_3SPbI_3$ (from −5 to ca. −100 °C) is yellow, as well, whereas the *γ*-phase (below ca. −100 °C) is white. Unfortunately, the material suffers from intense diffuse scattering at low temperatures, which hinders the crystal structure determination. Rietveld refinement was performed only for the pattern collected at room temperature, and the results are in good agreement with the corresponding single-crystal analysis (Figure S2). The SXPD patterns show a shift of the strongest diffraction peak (hkl = 0 1 0) from d = 8.293 Å at 22 °C, to d = 8.389 Å at −50 °C, and to d = 8.365 Å at −120 °C. At −120 °C, an additional small peak appears at ca. d = 8.1 Å. The last pattern collected at room temperature is identical to the original pattern at this temperature, which proves the full reversibility of the phase transitions. This is in contrast to *δ*-

DOI: 10.1021/acs.inorgchem.7b00395
Inorg. Chem. 2017, 56, 6302−6309

$FAPbI_3$, which converts only slowly from α-$FAPbI_3$ back to δ-$FAPbI_3$.[34]

The room temperature crystal structure of $(CH_3)_3SPbI_3$ as determined from SXPD analysis was subject to local optimization with DFT/PBEsol. The preference for the C_{3v} symmetry axis of the $(CH_3)_3S^+$ cation to lie in c direction was maintained. The average calculated Pb−I bond length of 3.214 Å compares well to the measured value of 3.21(1) Å. The bulk modulus was calculated from a fit to an equation of state at 6.5 GPa, as anticipated for a rather compressible 1D structure. For comparison, the theoretical bulk modulus for the defect perovskite Cs_2SnI_6 is 4.68 GPa,[38] whereas for the 3D $MAPbI_3$, it is over 10 GPa[39] (values depend largely on the computational method).

In order to better understand the crystal structure, the tolerance factor (t) for the ABX_3 perovskite structure was estimated. For such a calculation with $(CH_3)_3S^+$ in the A position, the ionic radius of $(CH_3)_3S^+$ is necessary. This cannot be found with high accuracy due to the nonspherical form of the trimethylsulfonium cation. However, considering that this cation adopts a trigonal pyramidal structure with C−S bond length of 180 pm and C−S−C angle of 103°[40] and by performing simple geometrical calculations, the distance of S from the center of mass of the molecule is

$$\frac{3m_{CH_3}}{3m_{CH_3} + m_S}\sqrt{1 - \frac{4}{3}\sin^2\left(\frac{103^o}{2}\right)}180\text{ pm} = 60\text{ pm}$$

By adding to this value the ionic radius of S^{2-} (184 pm) according to ref 41, the effective ionic radius of $(CH_3)_3S^+$ becomes $r(A) = 244$ pm. Given that $r(Pb) = 119$ pm and $r(I) = 220$ pm, $t = (r(A) + r(I))/\sqrt{2}(r(Pb) + r(I)) = 0.97$. Values of t close to 1 usually lead to low-dimensional perovskite structures with organic layers separating layers of inorganic octahedra.

3.2. Chemical and Thermal Stability. Regarding chemical stability, the new perovskite compound is stable in air even after several months and does not dissolve or react with water. Moreover, XRPD analysis of the sample after exposure to 85 °C for 1 day in ambient air shows no signs of degradation. For comparison, other organic lead halides, such as $MAPbI_3$,[42] decompose readily into PbI_2 at 45 °C (Table 2), whereas the orthorhombic modification of $CsPbI_3$ is relatively stable at 45 °C. This major difference in chemical reactivity between trimethylsulfonium cation and protonated amine cations is attributed to the absence of labile protons that in the case of the N−H bonds initiate hydrolysis reactions with moisture in the air. In this context, it was theoretically predicted that the use of non-amine protonated cations (e.g., $CH_3PH_3^+$, $CH_3SH_2^+$, and SH_3^+) in $APbI_3$ will strengthen the hydrogen bonding between A and $[PbI_6]$ octahedra and will ultimately improve the chemical stability of the compounds.[43] It was also recently observed that doping $CH_3NH_3PbI_3$ with methanethiol (CH_3SH) increases significantly the PCE and the chemical stability of the solar cell.[44]

Table 2. Comparison of Physical and Chemical Properties at Room Temperature for $APbI_3$ Perovskites with Various Cations (A)

compound	crystal system	E_g (eV)[22]	stability in air
$CsPbI_3$	cubic (3D)	1.73	unstable (converts to the orthorhombic phase)
	orthorhombic[a] (1D)	3.05	stable
$MAPbI_3$	tetragonal (3D)	1.61	moderately stable (decomposes slowly into PbI_2)
$FAPbI_3$	trigonal (3D)	1.48	unstable (converts to the hexagonal phase)
	hexagonal (1D)	3.0−3.3	moderately stable (decomposes slowly into PbI_2)
$(CH_3)_3SPbI_3$	hexagonal (1D)	3.1	stable

[a] $[PbI_6]$ octahedra form double chains, in contrast to $FAPbI_3$ and $(CH_3)_3SPbI_3$, where $[PbI_6]$ octahedra form single chains. For this modification, the band gap is taken from ref 45, assuming excitonic absorption.

DSC for $(CH_3)_3SPbI_3$ shows two reversible effects below room temperature, typical for first-order structural phase transitions (Figure 4a). The transition temperatures are determined by the onset average of the curves upon heating (endothermic effect) and cooling (exothermic effect) at −98 and −5 °C. The transition at −5 °C shows only small hysteresis of less than 1 °C, whereas the other transition shows rather large hysteresis, with onsets at −85 °C (heating step) and −112 °C (cooling step). Above 200 °C, the perovskite gradually decomposes into PbI_2 and volatile organic species (Figure 4b). This DSC residue was identified using XRPD analysis as pure PbI_2 with its characteristic thermochromic change from yellow to orange-red upon heating.

3.3. Optoelectronic Properties. The electronic absorption spectrum (Figure 5) shows readily resolved features below the band gap, which are characteristic for low-dimensional perovskite structures[14] and imply excitonic absorption at 411 nm with high binding energy that is stable at room temperature. Such excitonic peak energy is attributed to the PbI_3 chain network in several studies.[46,47] Analyzing the diffuse absorbance data, we get an E_g at 3.1 eV (interception of extrapolated line with energy axis in Figure 5). Such high band gap values are accordingly estimated in other 1D perovskites such as [tetrabutylammonium][PbI_3][48] (2.76 eV), $CsPbI_3$[49] (3.05 eV), or even $(CH_3)_3NHGeI_3$[50] (2.88 eV).

First-principles DFT calculations permitted the determination of the electronic band structure of the $(CH_3)_3SPbI_3$ perovskite. Figure 6 shows significant dispersion associated with the face-sharing networks of $[PbI_6]$ octahedra along ⟨001⟩ but flat bands in other directions. The static dielectric tensor also shows this anisotropy with calculated values of $\varepsilon^{xx} = 5.64$, $\varepsilon^{yy} = 5.05$, and $\varepsilon^{zz} = 12.14$. The obtained values (2.57 eV indirect and 2.59 eV direct) are smaller than those found in the corner-sharing perovskite frameworks, owing to the lack of structural flexibility associated with the more rigid face-sharing framework present here.

$(CH_3)_3SPbI_3$ has an electrical resistivity of $\rho \approx 8 \times 10^8$ Ω cm along the crystallographic c axis, as determined for a needle-shaped crystal grown from a DMF solution, classifying it as a semiconducting material (Figure 7a). The resistivity perpendicular to the c axis, measured on a plate-like single-crystal grown from an HI solution, was found to be approximately 4 times higher, $\rho \approx 3 \times 10^9$ Ω cm, showing also a moderate degree of polarization, consistent with the absence of chemical bonding between the 1D hexagonal stacks (Figure 7b). The high resistivity of the compound is attributed to its wide band gap and its 1D crystal structure, which produces less disperse electronic bands with relatively lower mobilities with respect to the intermediate band gap 3D perovskite $MAPbI_3$. This result is

DOI: 10.1021/acs.inorgchem.7b00395
Inorg. Chem. 2017, 56, 6302−6309

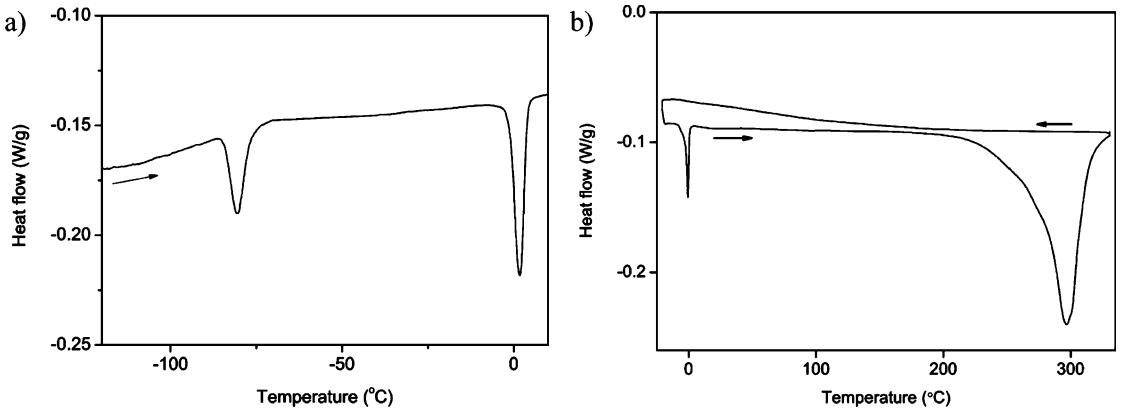

Figure 4. Differential scanning calorimetry for $(CH_3)_3SPbI_3$ over the temperature ranges of (a) −150 to 10 °C and (b) −20 to 330 °C (the sample decomposes gradually above 200 °C).

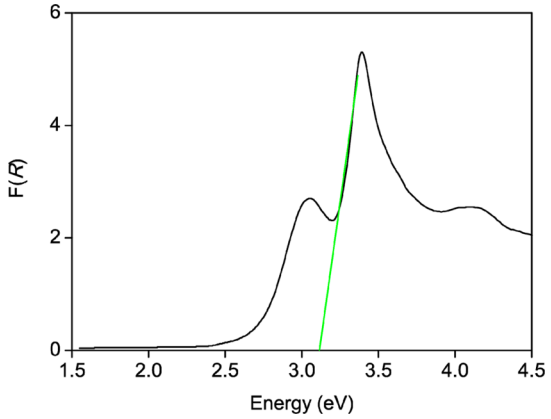

Figure 5. Diffuse reflectance UV−vis spectrum (in Kubelka−Munk units) for a $(CH_3)_3SPbI_3$ pellet. The crossover of the green line with the energy axis marks the optical band gap assuming excitonic absorption.

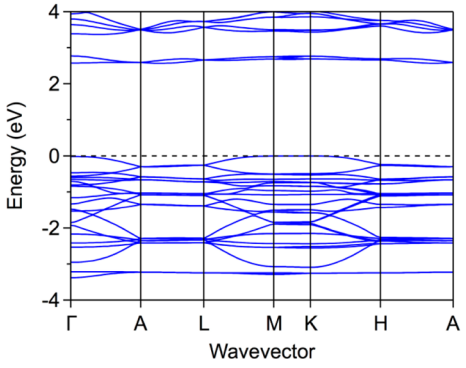

Figure 6. Electronic band structure of $(CH_3)_3SPbI_3$, plotted along the high symmetry lines of the first Brillouin zone, calculated using DFT/PBEsol including spin−orbit coupling.

in good agreement with other lower-dimensionality perovskites which produce similar electrical resistivity characteristics.[51]

Multi-temperature Raman spectra were collected on crystals of both $(CH_3)_3SPbI_3$ (Figure 8) and the organic precursor $(CH_3)_3SI$ (Figure S3) in order to gain further insight on to the local symmetry and the ordering of the organic cations. Both compounds are very stable under the 785 nm laser excitation. At room temperature, significant differences are observed in the vibrational frequencies of the trimethylsulfonium group below

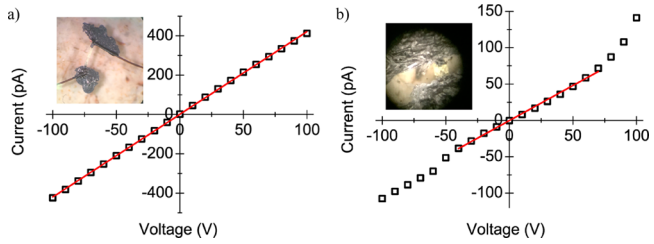

Figure 7. *I*−*V* plot for single crystals of $(CH_3)_3SPbI_3$ at room temperature. (a) Needle-shaped crystal from a DMF solution with dimensions (inset) 0.2 mm × 0.2 mm × 1.3 mm. (b) Plate-like crystal from an HI solution with dimensions (inset) 0.1 mm × 0.1 mm × 0.03 mm. The former crystal exhibits a regular ohmic behavior in the ±100 V range, whereas the latter shows signs of polarization above ±50 V.

1000 cm^{-1} upon coordination to the inorganic framework. Furthermore, distinct changes are observed in the Raman spectra across the phase transition temperatures for $(CH_3)_3SPbI_3$, which are absent in the corresponding spectra of $(CH_3)_3SI$. The strongest mode of the room temperature $(CH_3)_3SPbI_3$ spectra is observed at about 101 cm^{-1}. This cannot be correlated to any mode of the $(CH_3)_3SI$ compound, thus it is attributed to the A_{1g}-type symmetric stretching Pb−I vibration in accordance to ref 52. In fact, the strongest mode (101 cm^{-1}) is very well correlated to the A_{1g}-type symmetric stretching Pb−I vibration, where a strong band centered at 104 cm^{-1} was evidenced in the 1D $[C_6H_{14}N]PbI_3$, composed also by face-sharing $[PbI_6]$ octahedra.[53] A very broad band is observed at 40−70 cm^{-1}, which mainly comprises the E_g-type Pb−I stretching and T_{2g}-type in-plane bending I−Pb−I vibrations,[54] in combination with lattice modes.[55] The band is shown superimposed on an elastic scattering background continuum due to dynamic disorder of the organic cation.[56] With decreasing temperature below −20 °C and down to −100 °C, the 101 cm^{-1} mode does not show significant shift in frequency, indicating that the PbI_6 octahedra are hardly affected. On the contrary, the extensive 40−70 cm^{-1} band clears up from the elastic background and splits up into many resolved components, suggesting ordering of $(CH_3)_3S$ in conjunction with the crystal transformation from a disordered dynamic to a static crystal structure identified by X-ray analysis. Moreover, this first phase transition at −20 °C is combined with narrowing and blue shifting in frequency of the majority of phonon modes in accordance to the standard behavior expected by lattice contraction. Below −100 °C, the low-

DOI: 10.1021/acs.inorgchem.7b00395
Inorg. Chem. 2017, 56, 6302−6309

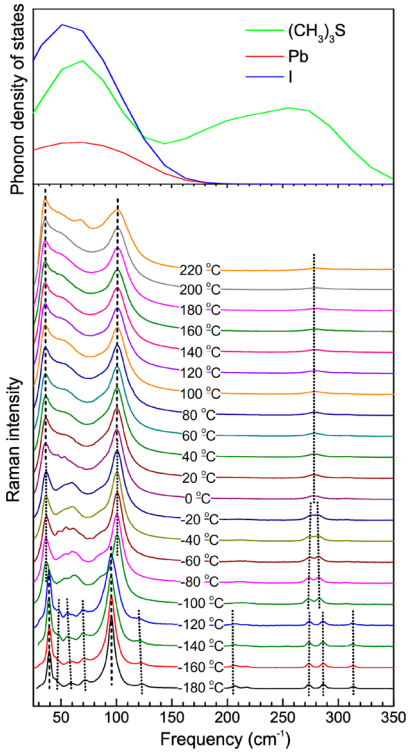

Figure 8. (Bottom) Multi-temperature Raman spectra with normalized intensities for $(CH_3)_3SPbI_3$. Dashed lines denote the shifts of certain peaks. (Top) Phonon density of states for $(CH_3)_3SPbI_3$ calculated within density functional perturbation theory with the PBEsol functional. The decomposition to molecular $(CH_3)_3S^+$ and PbI_3^- framework vibrations is determined by their contribution to the phonon eigenvectors.

frequency spectrum changes dramatically with the emergence of new Raman modes in the 10−350 cm^{-1} range and an abrupt negative shift of the 101 cm^{-1} peak to 95 cm^{-1}. The above changes mark the corresponding phase transformations of the perovskite to lower symmetry for the $[PbI_6]$ anion. At temperatures greater than 220 °C, the compound gradually decomposes into PbI_2 and the organic moieties evaporate.

The Raman data are in good agreement with calculations of the phonon density of states using density functional perturbation theory (Figure 8 and Figure S4). The calculated phonons at the center of the Brillouin zone cover the range from 0 to 3100 cm^{-1}, whereas the Pb−I contributions are confined in the 0−150 cm^{-1} range. There is significant overlap between $(CH_3)_3S^+$ vibrations within the crystal cavity and Pb/I vibrations at low frequencies. Similar behavior has been observed for $MAPbX_3$.[55] Apart from the Pb−I and lattice vibrations below 150 cm^{-1}, a very interesting behavior is observed for the temperature dependence of the Raman bands in the 270−320 cm^{-1} range. According to the Raman spectra of the $(CH_3)_3SI$ precursor (Figure S3) and the theoretically derived phonon density of states, which are included on the top of the experimental graphs in Figure 8, these bands solely involve SC_3 deformations of the organic cations. Above −20 °C, only a single broad peak is resolved in this range, at 278 cm^{-1}. Splitting of the band is observed below −20 °C and emergence of a new band at 313 cm^{-1}, below −100 °C. These spectral changes occur exactly at the phase transition temperatures, thus they can be directly related to the lowering in the symmetry of the crystallographic environment and in the ordering of $(CH_3)_3S$, upon decreasing temperature.

4. CONCLUSIONS

To our knowledge, $(CH_3)_3SPbI_3$ is the first structurally characterized sulfur-containing lead halide perovskite compound. The trimethylsulfonium cation is too large to fit in a 3D perovskite network, as found for α-, β-, and γ-$APbI_3$ phases (A = MA, FA). Instead, a 1D network of $[PbI_6]$ octahedra is formed, which leads to a relatively large band gap of 3.1 eV. Similar to the well-studied amine-containing $APbI_3$ perovskites, $(CH_3)_3SPbI_3$ undergoes reversible order−disorder phase transitions that are accurately investigated using X-ray diffraction and high-resolution Raman spectroscopy. More importantly, the compound exhibits high chemical stability in ambient air. In contrast to protonated amine cations, $(CH_3)_3S^+$ does not undergo a hydrolysis reaction and shows no signs of degradation in the air up to 85 °C. This novel approach of using hydrophobic organic cations may lead the way for more stable materials in perovskite solar cells if a 3D structure could be produced with a band gap of ca. 1.5 eV, as found for $MAPbI_3$ and $FAPbI_3$. Further investigations on the use of $(CH_3)_3SPbI_3$ in solar cells are in progress.

■ ASSOCIATED CONTENT

Supporting Information

The Supporting Information is available free of charge on the ACS Publications website at DOI: 10.1021/acs.inorgchem.7b00395.

Tables of atomic coordinates, thermal displacement parameters, bond lengths and angles for $(CH_3)_3SPbI_3$ at room temperature and −50 °C; SEM picture and photograph of needle-shaped $(CH_3)_3SPbI_3$ crystals grown in DMF solution; Rietveld refinement using SXPD data for $(CH_3)_3SPbI_3$ at room temperature; multi-temperature Raman spectra for $(CH_3)_3SI$; comparison between multi-temperature Raman spectra and calculated phonon density of states for $(CH_3)_3SPbI_3$ in the frequency range of 25−3200 cm^{-1} (PDF)

Accession Codes

CCDC 1547867−1547868 contains the supplementary crystallographic data for this paper. These data can be obtained free of charge via www.ccdc.cam.ac.uk/data_request/cif, or by emailing data_request@ccdc.cam.ac.uk, or by contacting The Cambridge Crystallographic Data Centre, 12, Union Road, Cambridge CB2 1EZ, UK; fax: +44 1223 336033.

■ AUTHOR INFORMATION

Corresponding Author

*Tel.: +30 210 650 3644. Fax: +30 210 651 1766. E-mail: p.falaras@inn.demokritos.gr.

ORCID

Andreas Kaltzoglou: 0000-0002-3093-9778
Constantinos C. Stoumpos: 0000-0001-8396-9578
Aron Walsh: 0000-0001-5460-7033
Mercouri G. Kanatzidis: 0000-0003-2037-4168
Polycarpos Falaras: 0000-0002-9553-5301

Author Contributions

The manuscript was written through contributions of all authors. All authors have given approval to the final version of the manuscript.

DOI: 10.1021/acs.inorgchem.7b00395
Inorg. Chem. 2017, 56, 6302−6309

Notes

The authors declare no competing financial interest.

■ ACKNOWLEDGMENTS

Financial support from FP7 European Union (Marie Curie Initial Training Network DESTINY/316494) as well as from "Advanced Materials and Devices for Collection and Energy Management" project within GSRT's KRIPIS action (MIS:452100), funded by Greece and the European Regional Development Fund of the European Union under NSRF 2007-2013 and the Regional Operational Program of Attica, is acknowledged. The work at Yonsei University was supported by the BK21+ programme, while the work at Imperial College London was supported by the Royal Society. Work at Northwestern University was supported by the Department of Energy, Office of Science, Basic Energy Sciences, under Grant SC0012541. We also acknowledge the provisional of beamtime at Diamond Light Source.

■ REFERENCES

(1) Glazer, A. M. Classification of Tilted Octahedra in Perovskites. *Acta Crystallogr., Sect. B: Struct. Crystallogr. Cryst. Chem.* **1972**, *28*, 3384−3392.
(2) Cohen, R. E. Origin of Ferroelectricity in Perovskite Oxides. *Nature* **1992**, *358*, 136−138.
(3) Salamon, M. B.; Jaime, M. The Physics of Manganites: Structure and Transport. *Rev. Mod. Phys.* **2001**, *73*, 583−628.
(4) Blatter, G.; Feigelman, M. V.; Geshkenbein, V. B.; Larkin, A. I.; Vinokur, V. M. Vortices in High-Temperature Superconductors. *Rev. Mod. Phys.* **1994**, *66*, 1125−1388.
(5) Nolas, G. S.; Kaeser, M.; Littleton, R. T.; Tritt, T. M. High Figure of Merit in Partially Filled Ytterbium Skutterudite Materials. *Appl. Phys. Lett.* **2000**, *77*, 1855−1857.
(6) Vassilakopoulou, A.; Papadatos, D.; Koutselas, I. Room temperature light emitting diode based on 2D hybrid organic-inorganic low dimensional perovskite semiconductor. *Applied Materials Today* **2016**, *5*, 128−133.
(7) Seth, S.; Mondal, N.; Patra, S.; Samanta, A. Fluorescence Blinking and Photoactivation of All-Inorganic Perovskite Nanocrystals $CsPbBr_3$ and $CsPbBr_2I$. *J. Phys. Chem. Lett.* **2016**, *7*, 266−271.
(8) Chung, I.; Lee, B.; He, J.; Chang, R. P. H.; Kanatzidis, M. G. All-solid-state Dye-sensitized Solar Cells with High Efficiency. *Nature* **2012**, *485*, 486−489.
(9) Stranks, S. D.; Eperon, G. E.; Grancini, G.; Menelaou, C.; Alcocer, M. J. P.; Leijtens, T.; Herz, L. M.; Petrozza, A.; Snaith, H. J. Electron-Hole Diffusion Lengths Exceeding 1 Micrometer in an Organometal Trihalide Perovskite Absorber. *Science* **2013**, *342*, 341−344.
(10) Burschka, J.; Pellet, N.; Moon, S. J.; Humphry-Baker, R.; Gao, P.; Nazeeruddin, M. K.; Grätzel, M. Sequential Deposition as a Route to High-performance Perovskite-sensitized Solar Cells. *Nature* **2013**, *499*, 316−320.
(11) http://www.nrel.gov/ncpv/images/efficiency_chart.jpg.
(12) Mitzi, D. B. Templating and Structural Engineering in Organic-inorganic Perovskites. *J. Chem. Soc. Dalton* **2001**, 1−12.
(13) Berdiyorov, G. R.; Kachmar, A.; El-Mellouhi, F.; Carignano, M. A.; El-Amine Madjet, M. Role of Cations on the Electronic Transport and Optical Properties of Lead-Iodide Perovskites. *J. Phys. Chem. C* **2016**, *120*, 16259−16270.
(14) Manser, J. S.; Christians, J. A.; Kamat, P. V. Intriguing Optoelectronic Properties of Metal Halide Perovskites. *Chem. Rev.* **2016**, *116*, 12956−13008.
(15) Gridunova, G. B.; Ziger, E. A.; Koshkin, V. M.; Lindeman, S. V.; Struchkov, I. T.; Shklover, V. E. A new quasi-unidimensional semiconductor - piperidinium triiodoplumbate. *Dokl. Akad. Nuak SSSR* **1984**, *278*, 656−660.
(16) Contreras, J. G.; Seguel, G. V.; Ungerer, B.; Maier, W. F.; Hollander, F. J. Triiodolead(II) Complexes, Structure and Raman Spectra. *J. Mol. Struct.* **1983**, *102*, 295−304.
(17) Krautscheid, H.; Vielsack, F. $[Pb_{18}I_{44}]^{8-}$ - An Iodoplumbate with an Unusual Structure. *Angew. Chem., Int. Ed. Engl.* **1995**, *34*, 2035−2037.
(18) Papavassiliou, G.; Koutselas, I.; Terzis, A.; Raptopoulou, C. P. Some Natural Three- and Lower-Dimensional Semiconductor Systems with Metal-Halide Units. *MRS Online Proc. Libr.* **1994**, *358*, 283−288.
(19) Tang, Z.; Guloy, A. M. A Methylviologen Lead(II) Iodide: Novel $[PbI_3^-]_\infty$ Chains with Mixed Octahedral and Trigonal Prismatic Coordination. *J. Am. Chem. Soc.* **1999**, *121*, 452−453.
(20) Tsai, H.; Nie, W.; Blancon, J.-C.; Stoumpos, C. C.; Asadpour, R.; Harutyunyan, B.; Neukirch, A. J.; Verduzco, R.; Crochet, J. J.; Tretiak, S.; Pedesseau, L.; Even, J.; Alam, M. A.; Gupta, G.; Lou, J.; Ajayan, P. M.; Bedzyk, M. J.; Kanatzidis, M. G.; Mohite, A. D. High-efficiency Two-dimensional Ruddlesden−Popper Perovskite Solar Cells. *Nature* **2016**, *536*, 312−316.
(21) Cao, D. H.; Stoumpos, C. C.; Farha, O. K.; Hupp, J. T.; Kanatzidis, M. G. Two-dimensional Homologous Perovskites as Light Absorbing Materials for Solar Cell Applications. *J. Am. Chem. Soc.* **2015**, *137*, 7843−7850.
(22) Chen, Q.; De Marco, N.; Yang, Y.; Song, T. B.; Chen, C. C.; Zhao, H. X.; Hong, Z. R.; Zhou, H. P.; Yang, Y. Under the Spotlight: The Organic-inorganic Hybrid Halide Perovskite for Optoelectronic Applications. *Nano Today* **2015**, *10*, 355−396.
(23) Lee, J. W.; Kim, D. H.; Kim, H. S.; Seo, S. W.; Cho, S. M.; Park, N. G. Formamidinium and Cesium Hybridization for Photo- and Moisture-Stable Perovskite Solar Cell. *Adv. Energy Mater.* **2015**, *5*, 1501310.
(24) Corey, E. J.; Chaykovsky, M. Dimethyloxosulfonium Methylide $((CH_3)_2SOCH_2)$ and Dimethylsulfonium Methylide $((CH_3)_2SCH_2)$ Formation and Application to Organic Synthesis. *J. Am. Chem. Soc.* **1965**, *87*, 1353−1364.
(25) Petříček, V.; Dušek, M.; Palatinus, L. Crystallographic Computing System JANA2006: General features. *Z. Kristallogr. - Cryst. Mater.* **2014**, *229* (5), 345−352.
(26) Spek, A. L. Structure validation in chemical crystallography. *Acta Crystallogr., Sect. D: Biol. Crystallogr.* **2009**, *65*, 148−155.
(27) Thompson, S. P.; Parker, J. E.; Potter, J.; Hill, T. P.; Birt, A.; Cobb, T. M.; Yuan, F.; Tang, C. C. Beamline I11 at Diamond: A New Instrument for High Resolution Powder Diffraction. *Rev. Sci. Instrum.* **2009**, *80*, 075107.
(28) Thompson, S. P.; Parker, J. E.; Marchal, J.; Potter, J.; Birt, A.; Yuan, F.; Fearn, R. D.; Lennie, A. R.; Street, S. R.; Tang, C. C. Fast X-ray Powder Diffraction on I11 at Diamond. *J. Synchrotron Radiat.* **2011**, *18*, 637−648.
(29) Roisnel, T.; Rodriguez-Carvajal, J. *Fullprof: A Program for Rietveld Refinement and Pattern Matching Analysis*, version Sept. 2012, France.
(30) Kubelka, P.; Munk, F. Ein Beitrag zur Optik der Farbanstriche. *Z. Technol. Phys.* **1931**, *12*, 593−601.
(31) Kresse, G.; Joubert, D. From Ultrasoft Pseudopotentials to the Projector Augmented-wave Method. *Phys. Rev. B: Condens. Matter Mater. Phys.* **1999**, *59*, 1758−1775.
(32) Blochl, P. E. Projector Augmented-Wave Method. *Phys. Rev. B: Condens. Matter Mater. Phys.* **1994**, *50*, 17953−17979.
(33) Perdew, J. P.; Ruzsinszky, A.; Csonka, G. I.; Vydrov, O. A.; Scuseria, G. E.; Constantin, L. A.; Zhou, X.; Burke, K. Restoring the Density-Gradient Expansion for Exchange in Solids and Surfaces. *Phys. Rev. Lett.* **2008**, *100*, 136406.
(34) Stoumpos, C. C.; Malliakas, C. D.; Kanatzidis, M. G. Semiconducting Tin and Lead Iodide Perovskites with Organic Cations: Phase Transitions, High Mobilities, and Near-Infrared Photoluminescent Properties. *Inorg. Chem.* **2013**, *52*, 9019−9038.
(35) Fabini, D. H.; Stoumpos, C. C.; Laurita, G.; Kaltzoglou, A.; Kontos, A. G.; Falaras, P.; Kanatzidis, M. G.; Seshadri, R. Re-entrant Structural and Optical Properties and Large Positive Thermal

DOI: 10.1021/acs.inorgchem.7b00395
Inorg. Chem. 2017, 56, 6302−6309

Expansion in a Hybrid Perovskite Lead Iodide. *Angew. Chem., Int. Ed.* **2016**, *55*, 15392−15396.
(36) Mancini, A.; Quadrelli, P.; Amoroso, G.; Milanese, C.; Boiocchi, M.; Sironi, A.; Patrini, M.; Guizzetti, G.; Malavasi, L. Synthesis, Structural and Optical Characterization of $APbX_3$ (A = Methylammonium, Dimethylammonium, Trimethylammonium; X = I, Br, Cl) Hybrid Organic-inorganic Materials. *J. Solid State Chem.* **2016**, *240*, 55−60.
(37) *International Tables of Crystallography*; Hahn, T., Ed.; Springer: The Netherlands, 2005; Vol. *A*, Space Group Symmetry, p 74.
(38) Kaltzoglou, A.; Antoniadou, M.; Kontos, A. G.; Stoumpos, C. C.; Perganti, D.; Siranidi, E.; Raptis, V.; Trohidou, K.; Psycharis, V.; Kanatzidis, M. G.; Falaras, P. Optical-vibrational Properties of the Cs_2SnX_6 (X = Cl, Br, I) Defect Perovskites and Hole-transport Efficiency in Dye-sensitized Solar Cells. *J. Phys. Chem. C* **2016**, *120*, 11777−11785.
(39) Egger, D. A.; Kronik, L. Role of Dispersive Interactions in Determining Structural Properties of Organic−Inorganic Halide Perovskites: Insights from First-Principles Calculations. *J. Phys. Chem. Lett.* **2014**, *5*, 2728−2733.
(40) Markham, G. D.; Bock, C. W. Structural and Thermodynamic Properties of Sulfonium Ions: an Ab Initio Molecular Orbital Study. *J. Phys. Chem.* **1993**, *97*, 5562−5569.
(41) Kieslich, G.; Sun, S. J.; Cheetham, A. K. Solid-state Principles Applied to Organic-inorganic Perovskites: New Tricks for an Old Dog. *Chem. Sci.* **2014**, *5*, 4712−4715.
(42) Misra, R. K.; Aharon, S.; Li, B.; Mogilyansky, D.; Visoly-Fisher, I.; Etgar, L.; Katz, E. A. Temperature- and Component-Dependent Degradation of Perovskite Photovoltaic Materials under Concentrated Sunlight. *J. Phys. Chem. Lett.* **2015**, *6*, 326−330.
(43) El-Mellouhi, F.; Marzouk, A.; Bentria, E. T.; Rashkeev, S. N.; Kais, S.; Alharbi, F. H. Hydrogen Bonding and Stability of Hybrid Organic−Inorganic Perovskites. *ChemSusChem* **2016**, *9*, 2648−2655.
(44) Li, H.; Yang, Y. G.; Feng, X.; Shen, K. C.; Li, H. Y.; Li, J.; Jiang, Z.; Song, F. Performance Improvement of $CH_3NH_3PbI_3$ Perovskite Solar Cell by CH_3SH Doping. *Nanomater. Nanotechnol.* **2016**, *6*, 62435.
(45) Kato, M.; Fujiseki, T.; Miyadera, T.; Sugita, T.; Fujimoto, S.; Tamakoshi, M.; Chikamatsu, M.; Fujiwara, H. Universal rules for visible-light absorption in hybrid perovskite materials. *J. Appl. Phys.* **2017**, *121*, 115501.
(46) Papavassiliou, G. C.; Mousdis, G. A.; Koutselas, I. B. Excitonic Bands in the Spectra of Some Organic-Inorganic Hybrid Compounds Based on Metal-Halide Units. *Synth. Met.* **2001**, *121*, 1339−1340.
(47) Papavassiliou, G. C.; Mousdis, G. A.; Raptopoulou, C. P.; Terzis, A. Preparation and Characterization of $[C_6H_5CH_2NH_3]_2PbI_4$, $[C_6H_5CH_2CH_2SC(NH_2)_2]_3PbI_5$ and $[C_{10}H_7CH_2NH_3]PbI_3$ Organic-Inorganic Hybrid Compound. *Z. Naturforsch.* **1999**, *54b*, 1405−1409.
(48) She, Y.-J.; Zhao, S.-P.; Tian, Z.-F.; Ren, X.-M. Inorganic−organic hybrid with one-dimensional face-sharing iodoplumbate chain showing novel dielectric anomaly and semiconductor emission. *Inorg. Chem. Commun.* **2014**, *46*, 29−32.
(49) Luo, P.; Xia, W.; Zhou, S.; Sun, L.; Cheng, J.; Xu, C.; Lu, Y. Solvent Engineering for Ambient-Air-Processed, Phase-Stable $CsPbI_3$ in Perovskite Solar Cells. *J. Phys. Chem. Lett.* **2016**, *7*, 3603−3608.
(50) Stoumpos, C. C.; Frazer, L.; Clark, D. J.; Kim, Y. S.; Rhim, S. H.; Freeman, A. J.; Ketterson, J. B.; Jang, J. I.; Kanatzidis, M. G. Hybrid Germanium Iodide Perovskite Semiconductors: Active Lone Pairs, Structural Distortions, Direct and Indirect Energy Gaps, and Strong Nonlinear Optical Properties. *J. Am. Chem. Soc.* **2015**, *137*, 6804−6819.
(51) Mao, L.; Tsai, H.; Nie, W.; Ma, L.; Im, J.; Stoumpos, C. C.; Malliakas, C. D.; Hao, F.; Wasielewski, M. R.; Mohite, A. D.; Kanatzidis, M. G. Role of Organic Counterion in Lead- and Tin-Based Two-Dimensional Semiconducting Iodide Perovskites and Application in Planar Solar Cells. *Chem. Mater.* **2016**, *28*, 7781−7792.
(52) Niemann, R. G.; Kontos, A. G.; Palles, D.; Kamitsos, E. I.; Kaltzoglou, A.; Brivio, F.; Falaras, P.; Cameron, P. J. Halogen Effects on Ordering and Bonding of $CH_3NH_3^+$ in $CH_3NH_3PbX_3$ (X = Cl, Br, I) Hybrid Perovskites: A Vibrational Spectroscopic Study. *J. Phys. Chem. C* **2016**, *120*, 2509−2519.
(53) Elleuch, S.; Abid, Y.; Mlayah, A.; Boughzala, H. Vibrational and Optical Properties of a One-Dimensional Organic−Inorganic Crystal $[C_6H_{14}N]PbI_3$. *J. Raman Spectrosc.* **2008**, *39*, 786−792.
(54) Nakamoto, K. *Infrared and Raman Spectra of Inorganic and Coordination Compounds, Part A, Theory and Applications in Inorganic Chemistry*, 6th ed.; Wiley: New York, 2009.
(55) Leguy, A. M. A.; Goñi, A. R.; Frost, J. M.; Skelton, J.; Brivio, F.; Rodríguez-Martínez, X.; Weber, O. J.; Pallipurath, A.; Alonso, M. I.; Campoy-Quiles, M.; Weller, M. T.; Nelson, J.; Walsh, A.; Barnes, P. R. F. Dynamic Disorder, Phonon Lifetimes, and the Assignment of Modes to the Vibrational Spectra of Methylammonium Lead Halide Perovskites. *Phys. Chem. Chem. Phys.* **2016**, *18*, 27051−27066.
(56) Yaffe, O.; Guo, Y.; Tan, L. Z.; Egger, D. A.; Hull, T.; Stoumpos, C. C.; Zheng, F.; Heinz, T. F.; Kronik, L.; Kanatzidis, M. G.; Owen, J. S.; Rappe, A. M.; Pimenta, M. A.; Brus, L. E. Local Polar Fluctuations in Lead Halide Perovskite Crystals. *Phys. Rev. Lett.* **2017**, *118*, 136001.

DOI: 10.1021/acs.inorgchem.7b00395
Inorg. Chem. 2017, 56, 6302−6309